

Invited paper

Comphy — A compact-physics framework for unified modeling of BTI

G. Rzepa^{a,*}, J. Franco^b, B. O'Sullivan^b, A. Subirats^b, M. Simicic^b, G. Hellings^b, P. Weckx^b,
M. Jech^a, T. Knobloch^a, M. Walti^a, P.J. Roussel^b, D. Linten^b, B. Kaczer^b, T. Grasser^a

^a Institute for Microelectronics, TU Wien, Austria

^b imec, Leuven, Belgium

ARTICLE INFO

Keywords:

Bias temperature instabilities
High- κ dielectric materials
Semiconductor device reliability

ABSTRACT

Metal-oxide-semiconductor (MOS) devices are affected by generation, transformation, and charging of oxide and interface defects. Despite 50 years of research, the defect structures and the generation mechanisms are not fully understood. Most light has been shed onto the charging mechanisms of pre-existing oxide defects by using the non-radiative multi-phonon theory. In this work we present how the gist of physical models for pre-existing oxide defects can be efficiently abstracted at a minimal loss of physical foundation and accuracy. Together with a semi-empirical model for the generation and transformation of defects we establish a reaction-limited framework for unified simulation of bias temperature instabilities (BTI). The applications of the framework we present here cover simulation of BTI for negative (NBTI) and positive (PBTI) gate voltages, life time extrapolation, AC stress with arbitrary signals and duty cycles, and gate stack engineering.

1. Introduction

The past 50 years of BTI research [1] and the numerous ongoing controversies [2] suggest that a) the underlying physical mechanisms are so diverse and complex that a rigorous description is barely feasible and b) the apparent phenomena are so peculiar that models without sound physical foundation can only cover a small range of observations. The controversies start with the role of dangling bonds at the oxide/channel interface: While it is commonly accepted that dangling bonds are created during stress, there are experimental studies which show that they do not dominate the degradation at BTI conditions [3, 4], opposed to what is typically assumed in reaction-diffusion (RD) models [5]. Attempts towards a rigorous description of charge trapping as an important contributor to BTI are based on the non-radiative multi-phonon (NMP) theory [6–8]. In particular, the 4-state NMP model [9] has been successfully applied to model various aspects of BTI [10, 11]. Hydrogen reactions were often linked to BTI and recently put into the context of NMP models [12]. However, given the complexity of this detailed physical model which tries to capture a number of peculiarities possibly not essential for life time prediction, many researchers employ simple power law descriptions which are used to fit the evolution of the threshold voltage shift ΔV_{th} as a function of stress time t_s , but have limited prediction accuracy and do not include recovery.

While there is certainly not a lack of BTI models in general, there still seems to be a gap between “detailed physical theory which is barely

applicable for practical purposes” and “practical approximations which miss important aspects of oxide degradation”.

In this paper we present an abstraction of the most elaborate findings from recent NMP studies [13–15] together with a semi-empirical model for defect generation and transformation and put them into a fast and easy-to-use framework we call “Comphy”, short for “compact-physics”. The core of this effort is the abstraction of the more complex multistate NMP processes to an effective 2-state model [16]. While this abstraction inevitably implies a slight loss in accuracy, which affects the switching behavior of individual defects, it still provides accurate results for the mean degradation and has a very limited number of effective *physical* parameters. It will be shown that this 2-state NMP model describes charging of oxide defects with “90% accuracy at 10% complexity” and is applicable across technologies and stress polarities.

As a fundamental prerequisite to any physical reliability model, we show in Section 2 how the electrostatics of MOS structures are computed based on the material parameters of the channel and the gate stack and we give a summary of the defect models used in Comphy. In Section 3 we apply Comphy to a) a commercial 130 nm SiON technology to confirm the correctness of the model for NBTI degradation under DC and AC stress b) a commercial planar 28 nm high- κ technology to discuss the NBTI and PBTI life time predictions, corroborated by a stress experiment covering 12 decades in stress time and c) to an imec technology targeting DRAM periphery devices with thick oxides to investigate the impact of gate stack engineering on PBTI and NBTI.

* Corresponding author.

E-mail address: rzepa@iue.tuwien.ac.at (G. Rzepa).

¹ Visiting imec.

Across all technologies we find very similar defect properties which enable unified modeling of NBTI and PBTI.

2. Modeling

The simulation of the threshold voltage V_{th} for arbitrary time-dependent gate voltages V_G and temperatures with Comphy is based on a description of the gate stack and channel properties as discussed in the first part of this section. It will be demonstrated that the mean degradation ΔV_{th} under all BTI conditions can be accurately captured by a 2-state NMP model and a simple double-well (DW) model as outlined in the second and third part of this section. The 2-state NMP model accounts for charging of pre-existing oxide defects featuring their distinct bias dependence as verified experimentally using the TDDS technique. In addition to charge trapping in pre-existing oxide defects which constitutes the *recoverable component*, another degradation mechanism is frequently observed which is pronounced at NBTI conditions and typically has large recovery times. The latter is often referred to as *permanent component* or *quasi-permanent component*. This component is typically ascribed to defect generation. However, the underlying physical mechanisms are less established. A simple double-well model with a field dependent energy barrier has been shown to capture the gist of experimental observations related to this component, at least at the present level of understanding.

For both defect models Comphy can compute the mean degradation in a deterministic fashion as well as the variability by Monte Carlo sampling of individual defects [16]. For fast computation of high-frequency long-term AC signals, Comphy features a dedicated AC mode [26] to simulate the degradation of the two BTI components.

As discussed in the following subsection, the charges of oxide defects can be considered self-consistently in the Poisson equation which allows for accurate simulations at high charge densities with Comphy. For example this is important for accurate prediction of the degradation at device end of life (typically 10 years).

Previously, we found that a uniform defect density in the interfacial layer of scaled high- κ technologies is a reasonable approximation to capture the degradation at BTI conditions [11]. However, our recent studies showed that this does not hold for technologies with thicker SiO₂ layers. From these technologies we deduce a significantly lower defect density further away from the channel interface. Accordingly, we approximate the defect density to be uniform in SiO₂ up to 0.6 nm away from the channel and neglect defects in SiO₂ which are further away from the channel.

When it comes to high- κ technologies with aggressively scaled interfacial layers in the range of 0.6 nm, the SiO₂ layer is merely a few atoms thick. To investigate the properties of such thin SiO₂ layers we employ DFT simulation. Using the scheme presented in [17] we create amorphous SiO₂ on top of crystalline Si (see Fig. 1, top). Computing the density of states for this structure shows that the band edges across this interface can be approximated by a ramp between Si and SiO₂ (see Fig. 1, bottom). Accordingly, device simulations with abrupt interfaces would underestimate the tunneling coefficients, in particular for technologies with thin SiO₂ layers. Similar results from DFT simulations were obtained by other groups on crystalline SiO₂, all indicating transition regions between Si and SiO₂ of about 0.4 to 0.6 nm [18–20]. In all Comphy simulations in this work we approximate this transition of the band edges with a 0.6 nm width which conveniently coincides with the region of high defect density in the SiO₂. Consistently, we also approximate the transition of the band edges between SiO₂ and HfO₂ with a ramp. Here we assume a transition region of 0.3 nm width [21], see Fig. 2.

2.1. Electrostatics

Physical oxide defect modeling is based on the carrier densities at the channel/oxide interface and the electrostatic potential across the

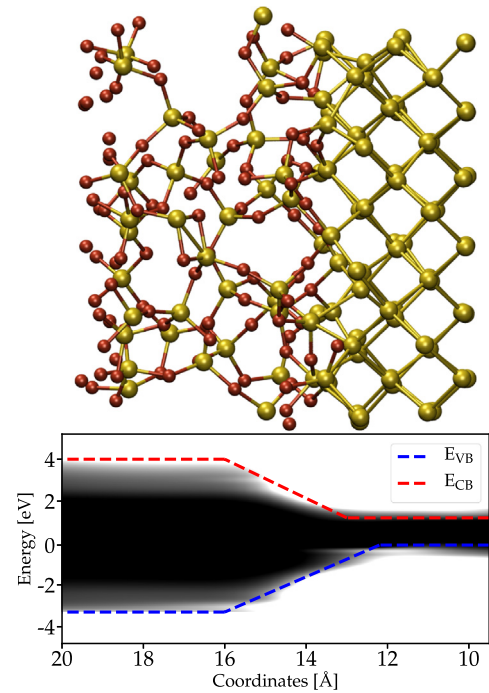


Fig. 1. **Top:** Amorphous SiO₂ on top of a crystalline Si created following the approach introduced in [17] with silicon atoms (yellow spheres) and oxygen atoms (red spheres). **Bottom:** DFT simulation of this structure shows a gradual change in the density of states indicating that the band edges across this interface can be approximated with ramps.

oxide. Comphy computes these values based on the input quantities listed in Table 1 and depicted in Fig. 3. As indicated by the references and respective equations in Table 2, we compute the temperature dependent band gap and effective masses following [24] and [22] to obtain the carrier concentrations using the Joyce-Dixon approximation [23]. Finally, the electrostatic potential is calculated iteratively by approximating the space charge following [25].

While all defaults are set for silicon channels, arbitrary channel materials can be used as long as the description by the implemented equations is sufficiently accurate.

Furthermore, the charges of the defects can be considered in the Poisson equation self-consistently (SCP). Since this is computationally expensive, as the Poisson equation has to be solved for every time step,

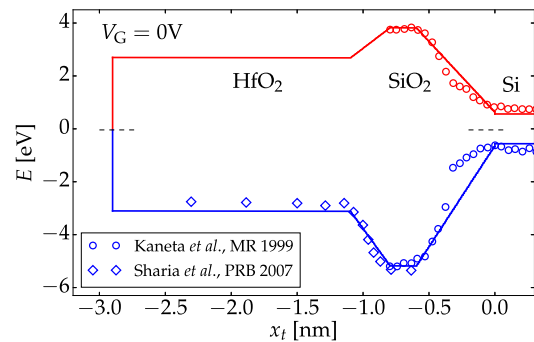


Fig. 2. Example for a band profile of a high- κ device. For additional accuracy, the transitional region at the Si/SiO₂ interface [18–20] and the SiO₂/HfO₂ interface [21] is approximated with a 0.6 nm and 0.3 nm wide ramp, respectively. As a reference, the results for the band edges from density functional theory studies are plotted for the Si/SiO₂ interface (circles: scaled in energy to fit the SiO₂ band gap) [18] and for the SiO₂/HfO₂ interface (diamonds) [21].

Table 1

Input quantities for computation of electrostatics in Comphy split in material parameters (upper part) and device specific parameters (lower part).

Input quantity	Ref.	Default	Unit
E_{G0}	[24]	1.206	eV
E_{G1}	[24]	$-2.73e-4 \times 10^{-4}$	eV/K
m_l	[24]	0.1905	1
m_{t0}	[24]	0.9163	1
$m_a \dots m_i$	[22]	See [22]	
N_{cv0}	[24]	$2.540933e25 \times 10^{25}$	m^{-3}
M_c	[24]	6	1
$\epsilon_{r,chan}$		11.68	1
$\epsilon_{r,oxide}$			1
$N_{a,chan}$			cm^{-3}
$N_{d,chan}$			cm^{-3}
ΔE_w			eV
x_{oxide}			m
V_G			V

Table 2

Quantities computed in Comphy.

Computed quantity	Ref.
$E_{G,chan}$	[24] Eq. 17
$m_{n,eff}$	[24] Eq. 6
$m_{p,eff}$	[22] Eq. 3
N_c	[24] Eq. 4
N_v	[24] Eq. 5
n_i	
$E_{f,bulk}$	
n_{bulk}	
p_{bulk}	
Q_s	[25]
V_s	[25]
E_{ox}	
φ	
$E_{f,chan}$	
n_{chan}	[23]
p_{chan}	[23]

there is also a non-self-consistent mode (NCP) which accounts for the reduction in electric field due to the oxide charges, but does not consider the impact on the occupancy of this reduction self-consistently. This is done by subtracting ΔV_{th} of the previous time step from V_G . Since this mode is already very accurate and much faster than the SCP mode, it is used as default in the following studies. Only the life time extrapolations are done with full accuracy using the SCP mode. The simulations using the dedicated fast AC mode, on the other hand, do not consider the reduction of the electric field due to oxide charges.

Note that since Comphy at this point is limited to BTI, the drain-source voltage is assumed to be zero which allows very efficient computation of a 1-dimensional cut.

Instead of calculating the surface potential V_s as shown in Fig. 3 the surface potential can also be given directly via an input table together with the Fermi level of the bulk. For example, this can be convenient for analysis using the CVC Hauser tool which computes the surface potential from CV curves [27] or other tools that compute the surface potential. However, the fixed surface potential is of course not compatible with the NCP or SCP mode.

2.2. NMP oxide defect model

The most fundamental properties of oxide defects are their spatial location x_T and their defect level E_T as depicted for a set of defects in Fig. 4, left. Defects below the Fermi level capture electrons and defects above the Fermi level emit electrons. However, for transient capture and emission events also the tunneling factors of the charge carriers and the energy barriers along the transition paths of the energy potential surface have to be considered [9]. For a 2-state defect this can be done efficiently using a harmonic approximation for the energy potential surface in both charge states 1 and 2 with the parabolic potentials

$$E_1 = E_{1,min} + c_1(q - q_1)^2, \quad (1)$$

$$E_2 = E_{2,min} + c_2(q - q_2)^2, \quad (2)$$

with the energy minimas $E_{1,min}$ and $E_{2,min}$ located at q_1 and q_2 and the curvatures c_1 and c_2 . For a semiclassical transition [29], it is sufficient to describe these parabolas with the ratio of the curvatures $R^2 = c_1/c_2$ and the relaxation energy $S = c_1(q_2 - q_1)^2$ as depicted in Fig. 4, right.

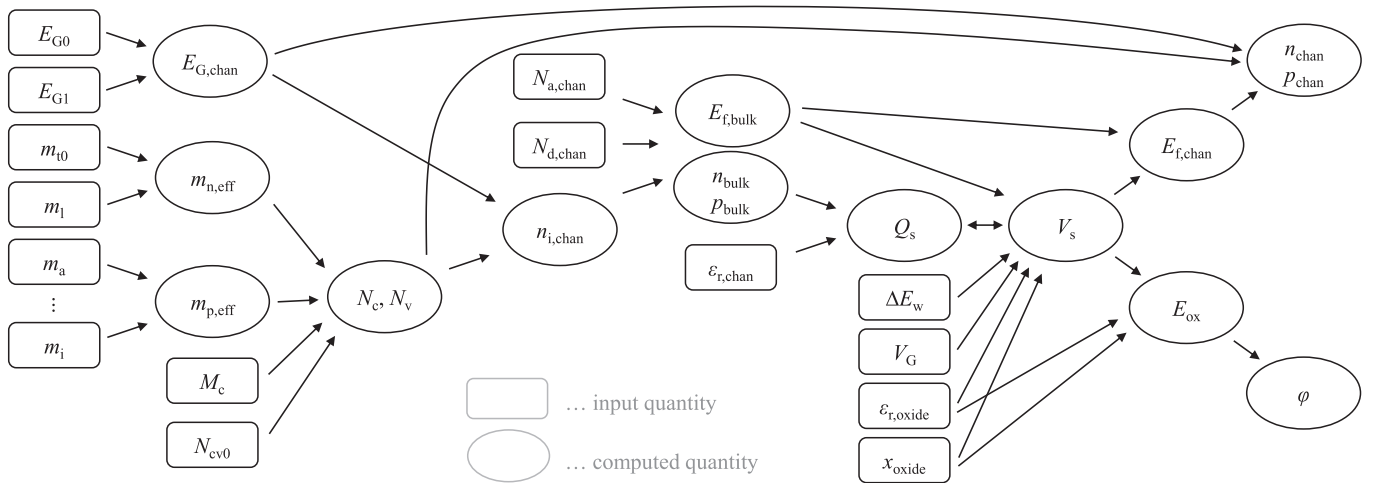


Fig. 3. Based on the input quantities (see Table 1) Comphy computes the carrier concentrations n and p as well as the electrostatic potential φ following [22–25] as indicated in Table 2.

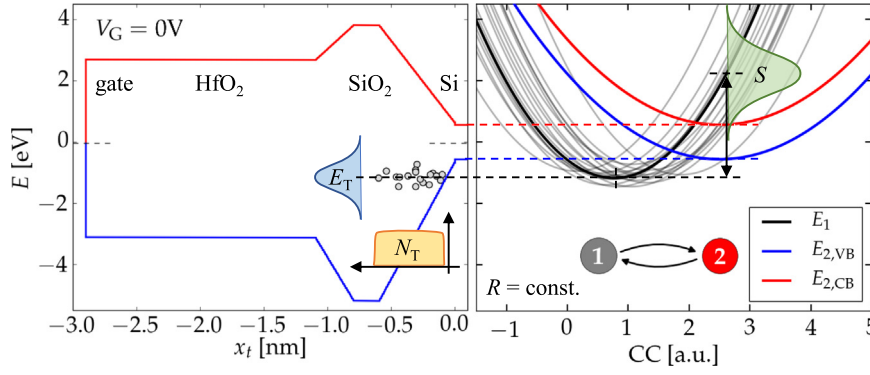


Fig. 4. The charge states of the defects are evaluated based on the device electrostatics and the individual parameters (E_T , x_T , S , R) of the discrete defects. **Left:** A band diagram of a pMOS with oxide defects depicted according to their interface distance and defect level (circles). **Right:** Configuration coordinate (CC) diagrams of the defects with the neutral state 1 and the positive state 2. The blue and red lines show the potential energy surface in state 2 for interaction with the valence and conduction band, respectively. The potential energy surface in state 1 is shown for the mean value (solid black line) and the discrete defects (grey lines) corresponding to the defects shown in the band diagram. The two-state model considers one effective NMP transition (state 1 \leftrightarrow 2) with the energy barrier ϵ_{12} for hole capture and ϵ_{21} for hole emission. To better illustrate the distribution of the relaxation energy S , the coordinates of the energy minimas of state 1 were shifted accordingly.

Table 3

Input quantities of the 2-state NMP model in Comphy. Values for various technologies are given in Table 7.

Input quantity		Unit
$\langle E_T \rangle \pm \sigma_{E_T}$	Norm. distr. trap level	eV
$\langle S \rangle \pm \sigma_S$	Norm. distr. relaxation energy	eV
R	Curvature ratio	1
N_T	Defect concentration	cm ⁻³
$x_{T,min}, x_{T,max}$	Spatial location of defect band	m

While R is approximated to be the same for all defects within a defect band, we assume the spatial distribution of defects within a defect band to be uniform with the defect density N_T , while E_T and S are assumed to be normally distributed (see Table 3).

In the classical limit, the intersection of these parabolas give the energy barriers ϵ_{12} from state 1 to 2 and ϵ_{21} from state 2 to 1 [9, 29]:

$$\epsilon_{12} = \frac{S}{(R^2 - 1)^2} \left(1 - R \sqrt{\frac{S + \Delta E_{12}(R^2 - 1)}{S}} \right)^2, \quad (3)$$

$$\epsilon_{21} = \epsilon_{12} - \Delta E_{12}, \quad (4)$$

with the energy difference $\Delta E_{12} = E_{2,min}(V_G) - E_{1,min}(V_G)$. $E_{1,min}$ is a function of E_T and of the electrostatic potential while $E_{2,min}$ is the energy of the carrier at the reservoir e.g. the channel or the gate. Note the removable singularity for linear electron-phonon coupling ($R = 1$) [9].

For the example of the reservoir being electrons at the conduction band edge of the channel, the rate for transitions from state 2 to state 1 is [30]

$$k_{21} = n v_{th,n} \sigma_{0,n} \vartheta_n e^{-\beta \epsilon_{21}} \quad (5)$$

where n is the concentration of electrons in the channel, $v_{th,n}$ their thermal velocity, $\sigma_{0,n}$ their capture cross section, ϑ_n their tunneling coefficient, and $\beta = 1/(k_B T)$. We approximate the capture cross sections to be constant and the same for electrons and holes for all oxide defects with a default value of

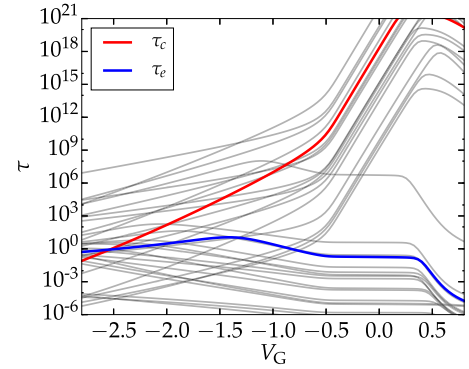


Fig. 5. Bias dependent capture and emission time constants of the defects of Fig. 4 at $T = 300$ K. The pronounced bias dependence and the wide distribution of time constants are in line with experimental studies [9, 28].

$$\sigma_0 = \sigma_{0,n} = \sigma_{0,p} = 2 \times 10^{-19} \text{ cm}^2 \quad (6)$$

Based on the rates the bias dependent capture and emission time constants can be calculated as

$$\frac{1}{\tau_c} = \sum_{r=1}^{N_R} k_{12,r}, \quad (7)$$

$$\frac{1}{\tau_e} = \sum_{r=1}^{N_R} k_{21,r}, \quad (8)$$

with the rates $k_{12,i}$ from state 1 to state 2 and the sum over r indicating the various charge carrier reservoirs (with R being the number of reservoirs) which may interact with the oxide defect. For MOSFETs with a metal gate the carrier reservoirs are typically

- The valence band of the channel,
- The conduction band of the channel, and
- The metal gate.

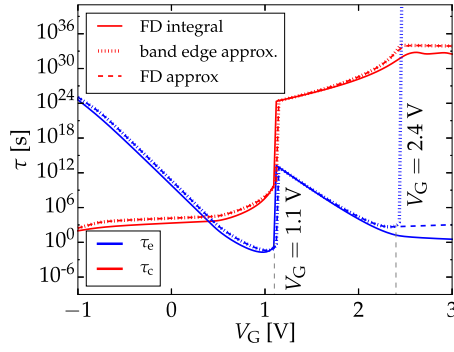


Fig. 6. The capture and emission time constants of a defect ($x_T = 2$ nm, $E_T = 0.7$ eV, $S = 0.5$ eV, $R = 0.4$) interacting with the channel of an nMOS with the same gate stack as shown in Fig. 4 at $T = 300$ K. Hole emission prevails at large V_G since τ_e becomes small. At $V_G = 1.1$ V there is a discontinuity in the time constants because there is no path along the parabolic potential energy surfaces for carriers from the conduction band (compare Fig. 7, left). Above $V_G = 2.4$ V also the transition for carriers from the valence band is not possible (compare Fig. 7, right) if all carriers are assumed to be located at the valence band edge (dotted line). However, the potential energy surfaces of carriers at higher energies can still have an intersection resulting in a finite barrier which can be computed with the integral in energy (solid line). This is captured by a more advanced Fermi-Dirac approximation (dashed line) summarized in Table 4.

The time constants for the defects shown in Fig. 4 are plotted in Fig. 5.

Assuming donor-like defects, the occupancy p_1 of the neutral state 1 and p_2 of the positive state 2 can be calculated based on $p_1 + p_2 = 1$ and the Master equation

$$\frac{dp_1(t)}{dt} = -p_1 \sum_{r=1}^{N_R} k_{12,r} + p_2 \sum_{r=1}^{N_R} k_{21,r} \quad (9)$$

again with the sum over all charge carrier reservoirs interacting with the oxide defect.

To compute ΔV_{th} based on these occupancies, the charge sheet approximation can be used. In this simple approximation, the oxide charge is assumed to be spread over a charge sheet with the interface distance x_T [31]. For single layer oxides with thickness t_{ox} , width W , and length L , ΔV_{th} evaluates to

$$\Delta V_{th} = -q_t \frac{t_{ox} \left(1 - \frac{x_t}{t_{ox}}\right)}{\epsilon_0 \epsilon_r W L} \quad (10)$$

where the charge of the oxide defect q_t is the product of the elementary charge and the occupancy of the positive charge state. For gate stacks with multiple layers a more general form of this equation is used.

In the above expressions it was assumed that the carriers are located at the band edges. A more accurate computation of the rates for the example of electrons is obtained by considering the density of states (D_n) and the distribution function of the carriers (f_n) in an integral over the energy as

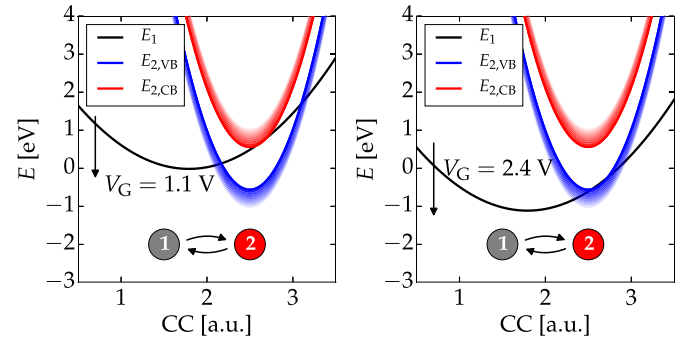


Fig. 7. The CC diagrams for the defect shown in Fig. 6. While there is no intersection with carriers in the conduction band below $V_G = 1.1$ V (left), excited carriers in the valence band still have a finite barrier even above $V_G = 2.4$ V (right).

Table 4

Barrier in the weak electron-phonon coupling regime in the Fermi-Dirac approximation in Comphy.

ΔE_{12}	ϵ_{12} (val. band)	ϵ_{12} (cond. band)	ϵ_{12} (metal)
> 0 eV	ΔE_{12}	Eq. 3	ΔE_{12}
< 0 eV	Eq. 3	0 eV	0 eV

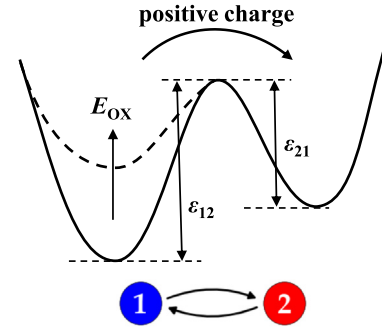


Fig. 8. The double-well model has two charge states separated by the thermal barriers ϵ_{12} and ϵ_{21} , where the former depends on the electric field E_{ox} .

$$k_{21}(E, E_T) = \int_{E_c}^{\infty} D_n f_n \Theta_n f_{21} dE \quad (11)$$

where $f_{21}(E)$ is the lineshape function [32].

As shown in Fig. 6, the band-edge approximation given in Eq. (5) is reasonable in the regime of strong electron-phonon coupling where the parabolas of the potential energy surfaces intersect between the minimas. However, if the ratio of the curvatures is such that there is no intersection of the parabolas above a certain V_G in the weak electron-phonon coupling regime (where the parabolas do not intersect between the minimas, see Fig. 7), the band-edge approximation fails to describe the transition rates. Since the computation of the rates with the energy

Table 5
Input quantities of the double-well model in Comphy.

Input quantity		Default	Unit
$\langle \varepsilon_{12,0} \rangle \pm \sigma_{\varepsilon_{12,0}}$	norm. distr. activation barrier	2.5 ± 0.5	eV
$\langle \varepsilon_{21} \rangle \pm \sigma_{\varepsilon_{21}}$	norm. distr. passivation barrier	2.0 ± 0.5	eV
k_0	transition rate for zero barrier	1×10^{13}	s^{-1}
γ	field dep. of activation barrier	5×10^{-10}	eV \cdot m/V
N_{it}	defect concentration	5×10^{13}	cm^{-2}

integral is computationally expensive, we employ an efficient approximation of the barriers in the weak electron-phonon coupling regime (listed in Table 4). As shown in Fig. 6, this approximation gives much better results and is nearly as efficient to compute as the simple approximation which only considers carriers at the band edges.

2.3. The “quasi-permanent” component

There are several degradation mechanisms in MOS structures which are not covered by charging of pre-existing oxide defects as described by the 2-state NMP model:

- Generation and annealing of oxide defects
- Activation and passivation of dangling bonds
- Transformation of existing oxide defects (H relocation)
- Metastability of pre-existing oxide defects

Which of these mechanisms dominates the quasi-permanent component depends on the processes and stress conditions and is currently debated. The assumption of activation of dangling bonds at BTI conditions is frequently made [5] but is in contradiction with experimental studies [3].

In the following we introduce a simple double-well (DW) model which describes the quasi-permanent component reasonably well on a phenomenological basis. The physical correspondence of this model is probably related to hydrogen relocation but remains speculative at this point. Interpreting, refining or replacing this model with a physical model is the subject of future work.

The DW model has two charge states separated by the thermal barrier ε_{12} for charging positively and ε_{21} for charging neutrally as depicted in Fig. 8. While the latter is an input quantity in Comphy, the former depends on the electric field E_{ox} and the input quantities γ and $\varepsilon_{12,0}$ as

$$\varepsilon_{12} = \varepsilon_{12,0} - \gamma E_{ox}. \quad (12)$$

Based on these barriers, the rates are computed with the input quantity k_0 using Boltzmann factors:

$$k_{12} = k_0 e^{-\beta \varepsilon_{12}}, \quad (13)$$

Table 6

Oxide material parameters used in these studies. E_{off} is given w.r.t. mid gap of the channel. Values based on [33].

Input quantity		SiO ₂	SiON	HfO ₂	Al ₂ O ₃	Unit
E_G	Band gap	9.0	9.0	5.8	7.0	eV
E_{off}	Valence band edge	−5.21	−5.21	−3.162	−3.6	eV
m_t	Tunnel mass	0.35	0.35	0.17	0.17	1
ε_r	Rel. permittivity	3.9	6.0	20	9.1	1

$$k_{21} = k_0 e^{-\beta \varepsilon_{21}}. \quad (14)$$

With these rates the transient occupancies of the two states can be computed in the same way as those of the 2-state NMP model described in the previous subsection. The impact on ΔV_{th} can then be evaluated by weighting these occupancies with the interface state density N_{it} (compare Eq. 10). Table 5 summarizes the input quantities of the DW model and their distributions.

3. Application

Comphy 1.0 is used throughout this work and all simulations can be fully reproduced using the material and defect parameters given in Tables 6 and 7 (in the Appendix). The following assumptions are used throughout all simulations presented in this work.

- The reduction of the electric field due to the charges in the oxide is considered, except for simulations using the dedicated fast AC simulation mode.
- pMOS and nMOS devices of the same technology are simulated with the same set of defects.
- For accurate and fast computation of the mean degradation we sample the defect distributions on a grid. For the 2-state NMP model we sample in space with $\Delta x_T = 0.1$ nm and in energy with $\Delta E_T = \Delta S = 0.1$ eV. The energy barriers of the DW model are sampled with $\Delta \varepsilon_1 = \Delta \varepsilon_2 = 0.05$ eV. For both models, the tails of the normal distributions are cut off for probabilities below 0.001%. Note that in the band diagrams we depict a Monte Carlo sampling of the oxide defects for a more intuitive visualization.
- Based on the broad experimental data investigated here we extract two defect bands in SiO₂ and two in HfO₂. Simulations are always conducted consistently with all defect bands. However, in the band diagram plots we do not depict defect bands if they do not contribute to the degradation at the respective stress condition.
- When a charge transition is observed experimentally, a positive shift of V_{th} indicates electron capture of an oxide defect while a negative shift indicates the emission of an electron. However, it is difficult to determine whether a defect has donor-like or acceptor-like states. Since the main interest usually is with the difference of V_{th} , this does not matter much. However, when it comes to self-consistent simulation of oxide charges, the net charge of oxides is crucial. Since the net charge of pristine devices is usually found to be rather low [1], we assume that the shallow bands are acceptor-like and the deep bands are donor-like since this gives the smallest net charge.
- The channel parameters used in these studies are all set to their defaults as given in Table 1 except for the dopings and the work-function difference which were set based on CVC Hauser [27] fits of the respective CV curves. These values are given in the appendix together with the defect parameters in Table 7.
- The oxide material properties were approximated to be the same for all technologies (except for the thicknesses) and are given in Table 6.
- Defects interact with the valence and conduction band edge of the channel and with the metal gate. Poly gate depletion is neglected.
- The band edges at interfaces are approximated by ramps as described in Section 2.

In the following Comphy is applied and verified on three distinct technologies:

- In Subsection 3.1 a commercial 130 nm technology with a 2.2 nm

Commercial SiON 130nm NBTI

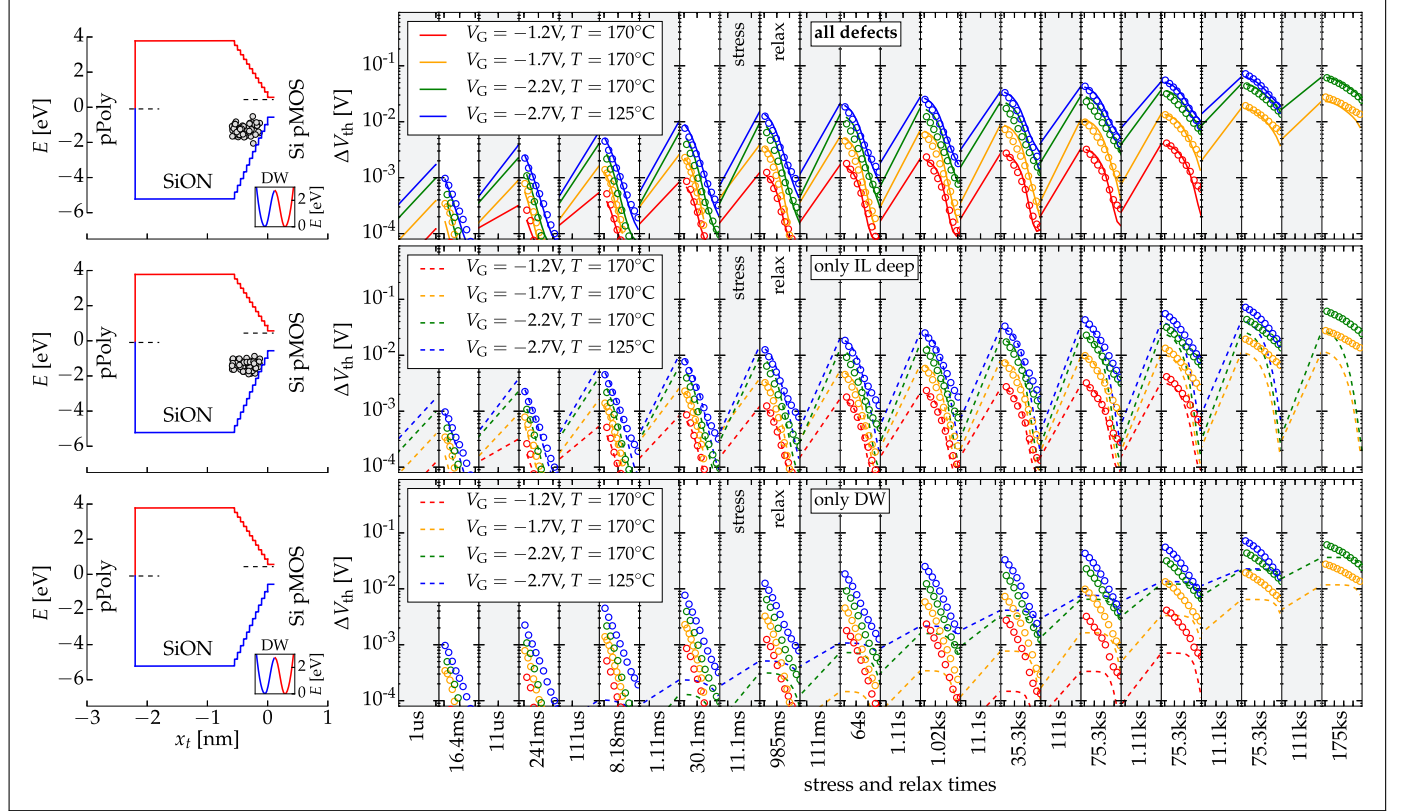


Fig. 9. Band diagrams plotted at flatband voltage (left) and the degradation of V_{th} during stress and recovery from experiments (circles) and Comphy simulations (lines) (right). Times are plotted on log scale with each phase starting at 0.1 μ s and the duration as given below. In the **upper panel**, all defects are simulated as indicated in the band diagram, while in the **middle panel** only NMP defects and in the **lower panel** only DW are considered.

thick SiON is investigated. Dedicated measurements are employed to calibrate the DW and the NMP model and the AC response is measured and simulated.

- In [Subsection 3.2](#) a commercial 28 nm high- κ technology is studied to predict the life time for NBTI and PBTI corroborated by long-term experiments.
- In [Subsection 3.3](#) implications of different oxide processes on devices with thick oxides as used in DRAM periphery logic are measured and simulated for both PBTI and NBTI.

While the first part is limited to NBTI on pMOS devices (PBTI is typically negligible for these technologies), the study of the other technologies comprises both, NBTI on pMOS and PBTI on nMOS devices.

3.1. NBTI degradation mechanisms and AC modeling

In this section, a commercial 130 nm technology with a 2.2 nm thick

SiON oxide is analyzed. As with all technologies, *all simulations in this subsection are done with the exact same Comphy parameters*. First, we apply the Comphy framework to the extensive MSM data previously obtained on a pMOSFET [38] with different stress voltages ($-V_G = 1.2, 1.7, 2.2, 2.7, 3.2$ V), temperatures ($T = 125$ and 170°C), and stress and recovery times in the range of 1 μ s–100 ks.

Some typical results from MSM experiments are shown in [Fig. 9](#). In order to verify the contributions of the NMP and the DW model we employ short pulses into accumulation after stress, as introduced previously [34]. Due to the distinct bias dependence of these two degradation mechanisms, this pulse discharges mainly NMP defects, allowing for a rough separation of the two components. As shown in [Fig. 10](#), the experimental features are captured well by the two models.

In [Fig. 11](#) the first recovery point of each MSM phase is plotted and compared to the degradation computed with Comphy for projected stress times up to 10^{10} s. The short measurement delay of 1 μ s is important for this comparison, as discussed in [Subsection 3.2](#). The agreement of experiment and simulation is good in general and also the

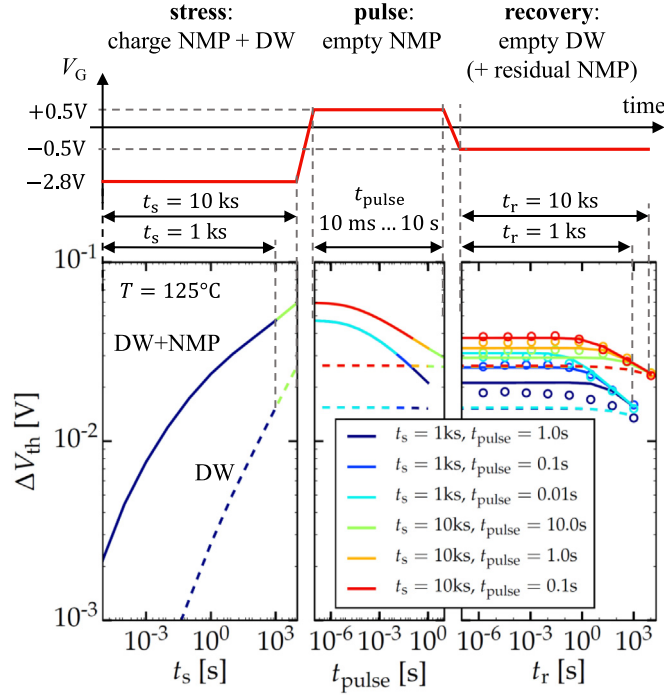


Fig. 10. This experiment is dedicated to separate the degradation described by NMP and DW models. A regular stress phase (left) is followed by a pulse into accumulation (middle). During this pulse, mainly defects described by the NMP model are discharged and the remaining degradation observed in the subsequent recovery (right) is mostly quasi-permanent. By varying the stress times t_s and the pulse duration t_{pulse} , two components can be separated. While the experimental data (circles) is subject to some device-to-device variability [34], the Comphy simulations (lines) capture all features observed.

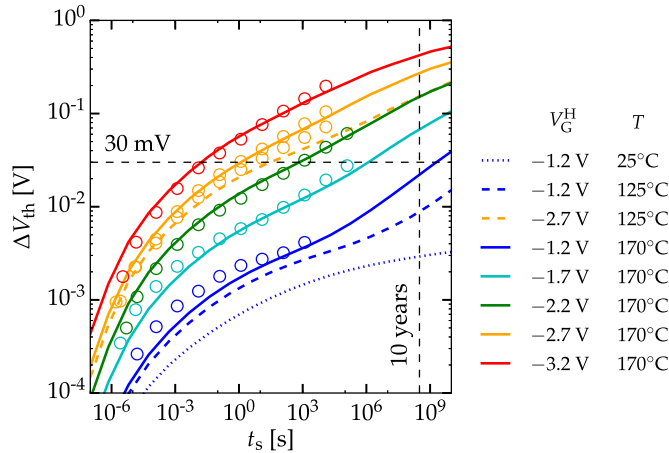


Fig. 11. Simulated stress for 10^{10} s with the parameters as extracted above (lines) plotted together with the degradation obtained from MSM experiments with 1 μ s delay (circles, no data available for -1.2 V at $T = 25$ and $T = 125^\circ\text{C}$). Because of the rather high activation energy, the quasi-permanent component is negligible at low temperatures. However, at higher temperatures and longer stress times there is a considerable increase in the time exponent due to this degradation mechanism. As explained in Subsection 2.3, the detailed physical mechanisms are not fully understood but the effective activation energy is confirmed by dedicated studies (see Fig. 10). The impact of the measurement delay and the life time extrapolation is discussed in Subsection 3.2.

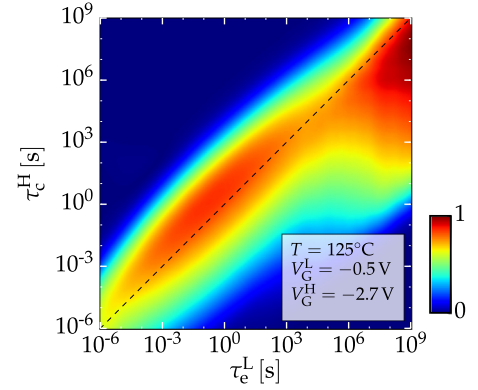


Fig. 12. The time constants of the 130 nm SiON technology depicted in a capture-emission time map. The capture times are given for stress ($V_G^H = -2.7$ V) while the emission times are given for recovery ($V_G^L = -0.5$ V), both at 125°C . While degradation at short stress times is dominated by 2-state NMP defects (lower left distribution), at large stress times the quasi-permanent component is more dominant with its large emission times (upper right distribution).

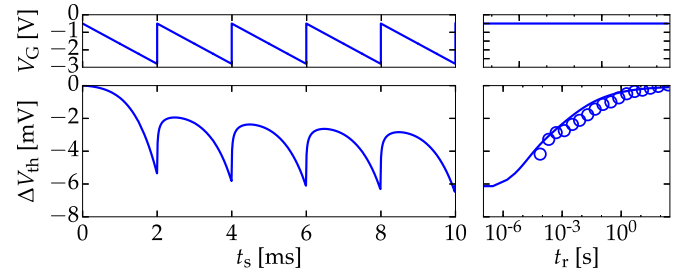


Fig. 13. The same commercial 130 nm SiON technology stressed with a saw tooth signal for 10 ms (500 Hz) (left) with subsequent recovery (right). Measurements are recorded during recovery (circles: [35]), while the full transient signal can be simulated with Comphy (lines in the bottom panels).

increase of the slope at longer stress times is captured by the simulations. This feature is pronounced at low voltages and high temperatures (for example for $V_G = 1.7$ V at $T = 170^\circ\text{C}$) and originates from the quasi-permanent component, which is activated at high temperatures but not overshadowed by the recoverable component at these low voltages.

Capture-emission time maps conveniently visualize the time constants of defects at given stress conditions [39]. These maps can be directly computed from MSM data as they are simply another way of visualization. However, also the time constants of the defects simulated with Comphy can be visualized in this same way, as shown in Fig. 12. Here the two contributions and their distinct properties become visible: Oxide defects described with the 2-state NMP model are more recoverable, hence are mostly above the main diagonal with shorter emission times on average. The quasi-permanent component on the other hand is mostly below the main diagonal and has in general longer time constants at the stress conditions used in Fig. 12.

An example for simulating arbitrary AC signals with Comphy is given in Fig. 13. The experiment simulated here starts with a saw tooth signal at 500 Hz followed by a recovery where the ΔV_{th} shift is recorded

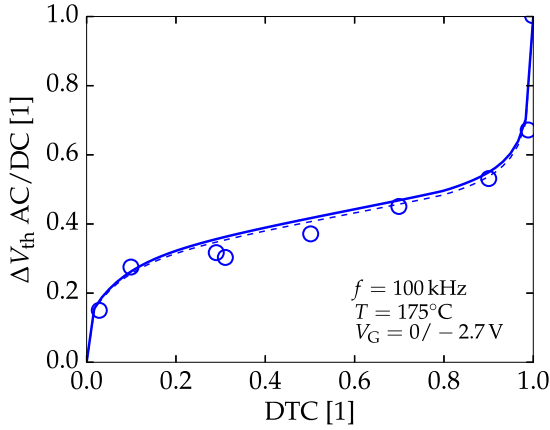


Fig. 14. The “S-shape” of the data published in [36] is reproduced by Comphy simulations on the previously calibrated commercial 130 nm SiON device. The simulations also consider the measurement delay of 1 μ s (solid line) and compare it to the degradation directly after stress (dashed line). At 100 kHz oxide defects show a distinct frequency dependence due to metastable states which is considered in the effective 2-state NMP model accordingly [37].

(data from [35]). Again the same model parameters were used to obtain good agreement to experimental data.

An “S-shape” is frequently reported for duty cycle dependences [36, 40]. To verify this with Comphy the experiment of [36] was simulated with the device calibrated above. At the frequency of 100 kHz used here, the multistate frequency dependence of oxide defects becomes important. This feature is not covered by regular 2-state models, however, the 2-state NMP model in Comphy features an analytic description to account for the increased capture time constants at high frequencies due to metastable states [37]. Using the time constants $\tau_{c1} = 1$ ms and $\tau_{e1} = 1$ μ s, which define the effect of the virtual third state in this description, a good agreement is obtained (see Fig. 14). For these simulations the dedicated fast AC simulation mode was used [26].

3.2. Life time extrapolation

For a detailed study of accurate life time extrapolation we have conducted a 3-month measurement on a commercial planar 28 nm high- κ technology (rapid thermal oxidation (RTO) interfacial layer, post deposition anneal (PDA) and TiN gate). Together with fast measurements with 1 μ s measurement delay and further MSM experiments at

Foundry planar 28 nm PBTI

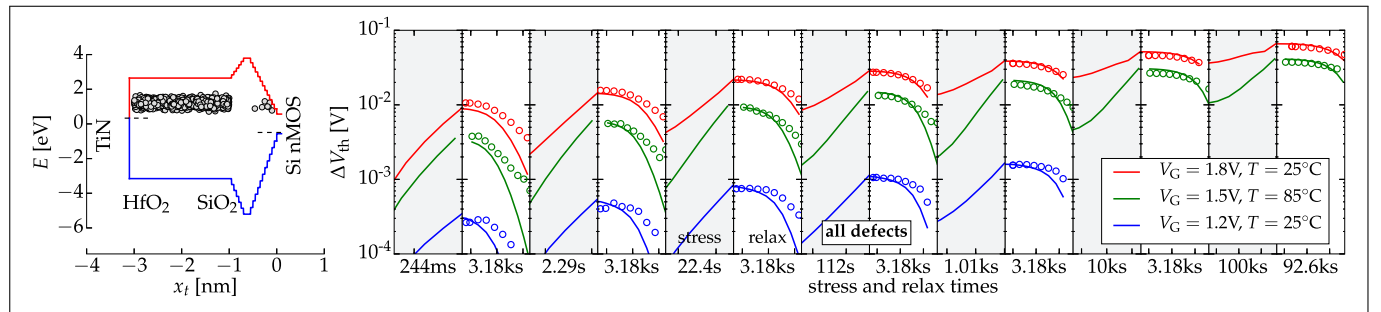


Fig. 15. Band diagram plotted at flatband voltage (left) and the ΔV_{th} during stress and recovery from experiments (circles) and Comphy simulations (lines) (right). Times are plotted on a logarithmic scale with each phase starting at 10 ms and the duration as given below. PBTI of this technology is governed by shallow oxide defects in the high- κ . Additionally, some fast traps are located in the interfacial layer, however, they barely affect the degradation.

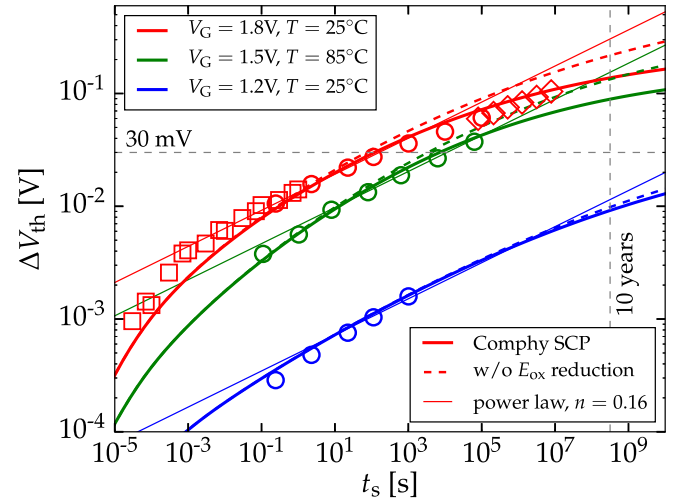


Fig. 16. Combining the first recovery points of the MSM data (circles) shown in Fig. 15 with data from experiments with 1 μ s measurement delay (rectangles) and a dedicated long term experiment (diamonds), gives degradation during stress spanning 12 decades in time. While the power law cannot fit this data, the Comphy simulations with oxide defects considered self-consistently in the Poisson equation (SCP) can very well reproduce the data consistently for different temperatures and voltages with the same model parameters.

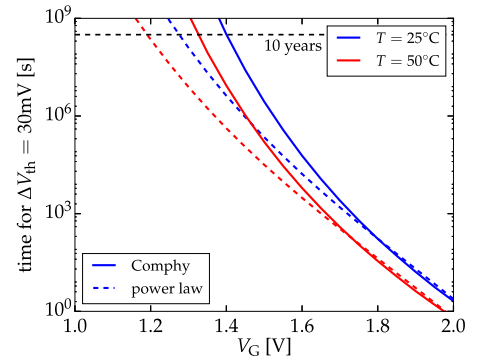


Fig. 17. The PBTI life time using a 30 mV criterion for the commercial planar 28 nm technology with the same parameters as used throughout Subsection 3.2. As shown in detail in Fig. 16 the power law gives a pessimistic life time extrapolation while the simulations with Comphy fit the stress data across 12 decades in time and allow a more accurate life time prediction.

Foundry planar 28 nm NBTI

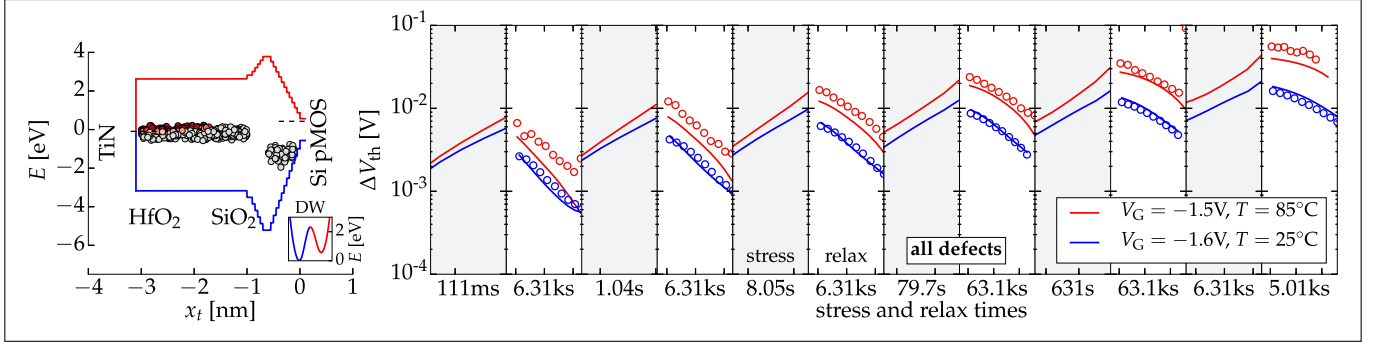


Fig. 18. Band diagram plotted at flatband voltage (left) and ΔV_{th} during stress and recovery from experiments (circles) and Comphy simulations (lines) (right). Times are plotted on a logarithmic scale with each phase starting at 10 ms and the duration as given below. NBTI of this technology is governed by deep oxide defects in the interfacial layer and by DW defects. Additionally, some deep traps in the high- κ layer give a small contribution to the degradation.

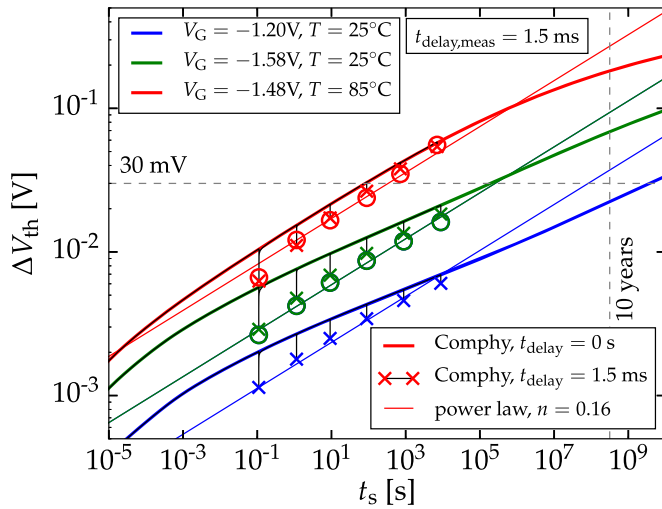


Fig. 19. The same data as in Fig. 18 but only the first measurement point of each relaxation phase is plotted as a function of the stress time (circles). Due to the fast recovery after NBTI stress, there is a substantial deviation from the Comphy simulations with stress only (thick lines). However, if the measurement delay is included in the Comphy simulations (thin lines and crosses) a good agreement with the data is obtained. A strong dependence of the obtained power law exponent on the measurement delay is apparent. While the power law with $n \approx 0.16$ fits the data with 1.5 ms measurement delay reasonably well, it is off substantially for shorter measurement delays as shown in Fig. 20.

different voltages and temperatures for NBTI and PBTI we were able to extract the defect properties of this technology with high accuracy. Considering the charges self-consistently in the Poisson equation in Comphy allows for accurate modeling including the reduction of the electric field. All simulations in this subsection are done with the same parameters as listed in the appendix in Table 7.

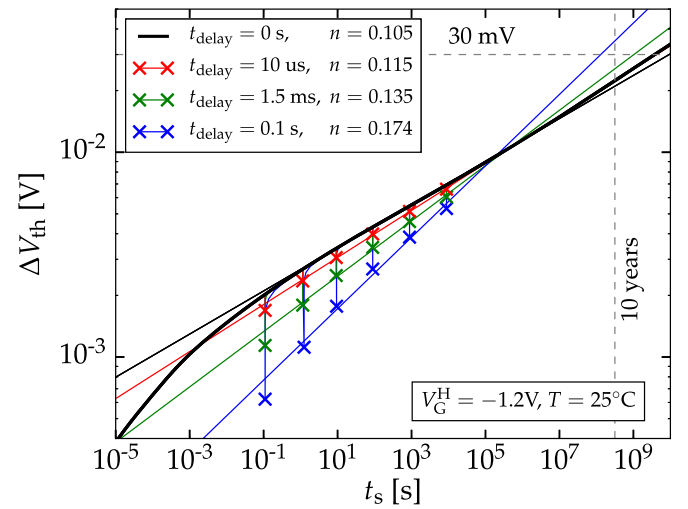


Fig. 20. The same setup as in Fig. 19 but simulated for different measurement delays. The extracted power law exponent varies between $n \approx 0.105$ and 0.174, which shows the significant impact of the measurement delay on life time extrapolations based on power law fits as shown in Fig. 21.

PBTI can be captured well with two NMP defect bands, one in the interfacial layer and one in the high- κ layer. In this technology, the latter governs the degradation at PBTI conditions which makes a precise calibration of the defects in the interfacial layer difficult. More suitable for an accurate calibration of these defects are devices with a thick SiO₂ layer as demonstrated in Subsection 3.3. We apply very similar parameters here accordingly to get a good agreement for the MSM data with up to 100 ks stress and 63 ks recovery shown in Fig. 15.

Combining the MSM data shown in Fig. 15 with stress experiments with 1 μ s measurement delay and with a long-term experiment gives

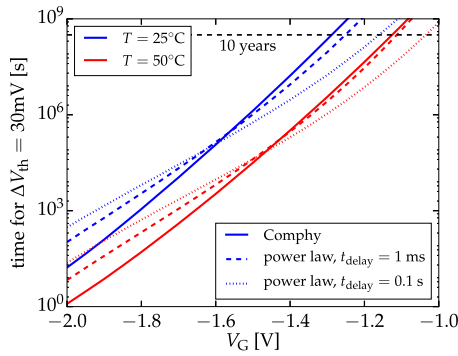


Fig. 21. The NBTI life time using a 30 mV criterion for the commercial planar 28 nm technology with the same parameters as used throughout Subsection 3.2. As shown in detail in Fig. 20 the extracted power law exponent depends on the measurement delay. An accurate life time prediction with power law extrapolations can only be obtained with short measurement delays, otherwise the power law gives pessimistic life time predictions.

degradation data covering 12 decades in time. As shown in Fig. 16 the NMP defects simulated with Comphy are in good agreement for all stress conditions across the full range of stress times. The effect of the reduction of the electric field due to the oxide charges is visible for larger degradation and has to be considered for accurate life time prediction. Some groups report a power law exponent for PBTI of $n \approx 0.16$ [41], however, this is only valid in a very narrow stress time window. For short stress times and long stress times the power law with $n \approx 0.16$ does not fit the data which leads to a significant underestimation of the life time as apparent in Fig. 16 and shown in detail in Fig. 17.

NBTI of the same commercial 28 nm technology is governed by different defects compared to PBTI. As shown in the previous NBTI study in Subsection 3.1, deep defects in the interfacial layer contribute to the degradation and the development of a quasi-permanent component is also observed. Additionally, a weak contribution of deep defects in the high- κ is deduced from detailed studies of this defect band on other technologies (see Subsection 3.3). These three components were optimized to fit the MSM data as shown in Fig. 18. The recovery after NBTI stress is quite different from recovery after PBTI stress (see Fig. 15). The fast recovery of the defects after NBTI stress makes the measurement delay after stress crucial for NBTI studies. Fig. 19 shows the long term stress for NBTI. In addition to simulations with constant stress, we also simulate the measurement procedure including the measurement delay. This results in good agreement with experimental data and shows the importance of the measurement delay. The same as for PBTI, some groups report a power law exponent of $n \approx 0.16$ if corrected for the measurement delay [42]. While this works reasonably well for the NBTI data of this commercial 28 nm technology with a measurement delay of 1.5 ms, there is a considerable deviation of this power law fit with $n \approx 0.16$ for shorter measurement delays as shown in Fig. 20. The impact of the measurement delay on the life time prediction is shown in Fig. 21. While the power law gives a reasonably

accurate life time estimation if based on measurements with short measurement delay, it gives a pessimistic estimation for longer measurement delays.

3.3. Gate stack engineering

The solid physical foundation of Comphy allows for insights into process dependences of oxide defects and enables path finding and gate stack engineering. In this subsection we analyze the oxide defects of devices with thicker oxides as used for DRAM periphery logic. While these technologies are substantially different from those analyzed in the previous sections, Comphy gives consistent results and captures all effects originating from different processes with HfO₂ and Al₂O₃ deposition, removal, and anneals for both, NBTI and PBTI.

Of particular interest in these studies is a phenomenon called “anomalous PBTI” which is typically observed on oxides with an additional thin oxide layer on top of the high- κ stack [43–45]. In the following we quantitatively confirm that this anomalous degradation is “due to charge exchange between the high- κ layer and the metal gate” as speculated in [44].

Starting with PBTI, a technology with a plain 5 nm thick in situ steam generated (ISSG) SiO₂ allows for characterization of the shallow defects in SiO₂. Because of their low defect density they give a weak PBTI response, but can be well calibrated as shown in the first part of Fig. 22. Next we characterize a technology with the same SiO₂ but with 20 cycles of atomic layer deposited (ALD) HfO₂ on top (corresponding to a thickness of about 2 nm) and a TaN/TiN metal gate without dedicated temperature treatments. Only minor effects of this processing step on the defects in the SiO₂ are expected and the considerable increase of degradation during PBTI can be traced back to defects in the HfO₂. Consistent with the studies in Subsection 3.2 we find two defect bands in the HfO₂ responsible for this degradation. In the commercial planar 28 nm technology, the deep band in the HfO₂ contributes to degradation at NBTI conditions, but not at PBTI conditions. This is different for the DRAM periphery technology because of the different alignment of the energies due to the thick SiO₂. These deep defects in the HfO₂ cause a peculiar feature which can be observed at the last recovery phase at high stress voltages in the second part of Fig. 22: After an initial recovery, the device degrades during the recovery phase. This is due to electron capture of the deep defects in the HfO₂ from the gate. This effect is more evident in the third part of Fig. 22 where we analyze the same technology but with additional 4 cycles of ALD Al₂O₃ (about 0.4 nm) on top of the HfO₂. Again, the oxide was not annealed, so there should be no significant diffusion in the oxide. While the Al₂O₃ layer itself has defect states, their impact will be rather small because the layer is very thin and far away from the channel. However, this layer changes the alignment of the deep defects in the HfO₂ and the Fermi level of the gate. This strongly supports the electron capture from the gate during recovery, which was rather weak previously. Together with the regular degradation caused by the shallow defects in the HfO₂ and SiO₂, a peculiar degradation is observed on these devices: At low stress voltages V_{th} shifts towards negative voltages and only at higher stress voltages the usual PBTI degradation of V_{th} towards positive voltages is observed.

imec DRAM periphery PBTI

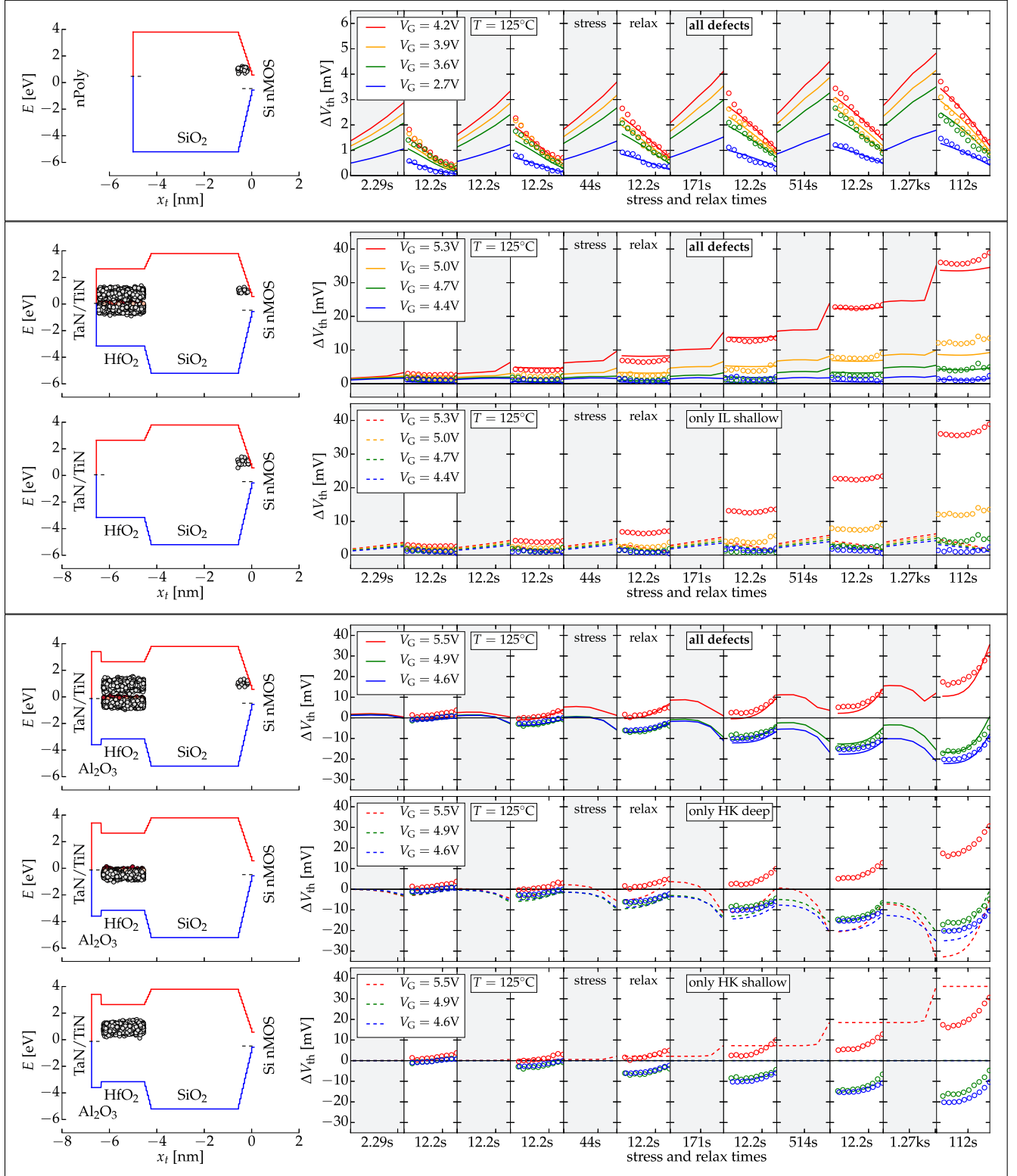


Fig. 22. Band diagrams plotted at flatband voltage (left) and ΔV_{th} during stress and recovery from experiments (circles) and Comphy simulations (lines) (right). Times are plotted on logarithmic scales with each phase starting at 1 ms and the duration as given below. The **1st panel** shows the degradation of a plain SiO_2 device. At PBTI conditions, this degradation is very weak because of the small defect density of shallow defects in the SiO_2 . The **2nd and 3rd panels** show the degradation of the same device as in the 1st panel but with 20 cycles of ALD HfO_2 on top. This additional layer causes a pronounced degradation for PBTI stress. The **4th, 5th and 6th panels** show the degradation of the same device but with additional 4 cycles of ALD Al_2O_3 after the 20 cycles HfO_2 ALD. While for electrostatic reasons this additional Al_2O_3 layer does not cause a significant degradation itself, it affects the alignment of defects in the HfO_2 with the Fermi level of the gate and thereby leads to an anomalous degradation [43–45].

imec DRAM periphery NBTI

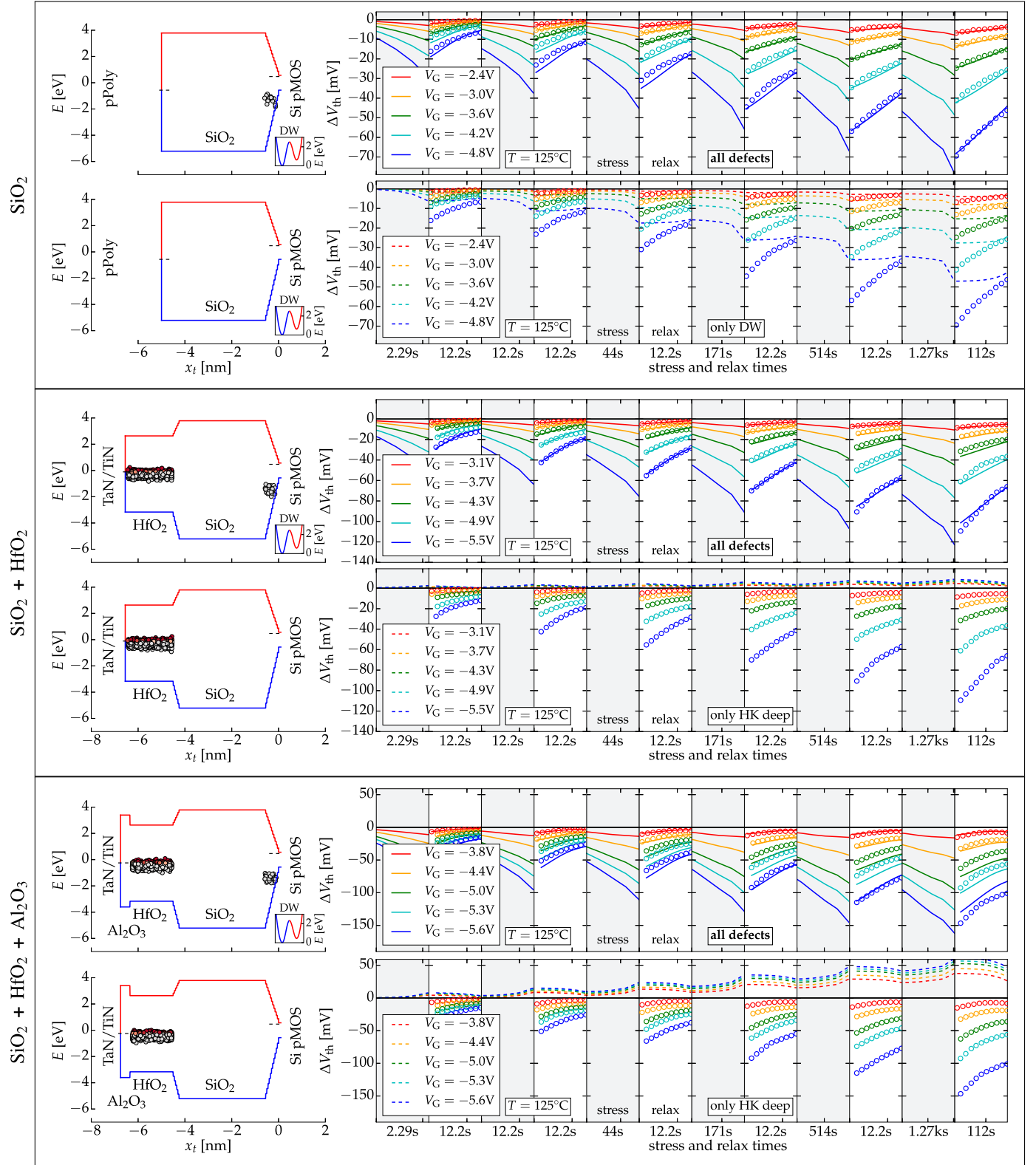


Fig. 23. Band diagrams plotted at flatband voltage (left) and ΔV_{th} during stress and recovery from experiments (circles) and Comphy simulations (lines) (right). Times are plotted on logarithmic scales with each phase starting at 1 ms and the duration as given below. The 1st and 2nd panels show the degradation of a plain SiO_2 device which is governed by deep defects in the SiO_2 and the degradation described by the double-well model. The 3rd and 4th panels show the degradation of the same device as in the 1st and 2nd panels but with 20 cycles of ALD HfO_2 on top. This additional layer causes further degradation because of the deep defect band in HfO_2 . The 5th and 6th panels show the degradation of the same device but with additional 4 cycles of ALD Al_2O_3 after the 20 cycles HfO_2 ALD. Similar to the case for PBTI, this additional Al_2O_3 layer does not cause a significant degradation itself but affects the alignment of defects in the HfO_2 with the Fermi level of the gate. However, at the NBTI conditions investigated here, the anomalous degradation cannot be observed directly because it is overshadowed by the regular degradation originating from defects in the SiO_2 . Still, there is evidence in the experimental data for this mechanism visible as a slight reversal in the last recovery phases at low stress voltages.

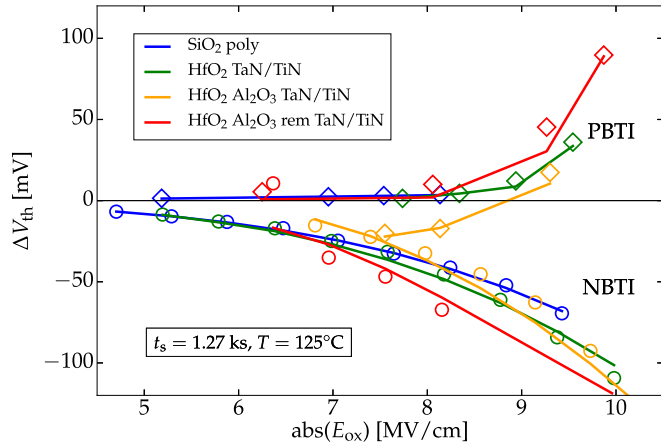


Fig. 24. The measured oxide field dependence of the degradation after 1.27 ks of stress (circles) is in good agreement with the simulations (lines) for all technologies for both, NBTI and PBTI. In the technology where the Al_2O_3 layer is in place, the alignment of the defects in the HfO_2 and the Fermi level of the gate is loosened. This causes an anomalous degradation which in the case of PBTI is so pronounced that a negative net degradation can be observed. After removal of the Al_2O_3 layer, this effect is reverted, all in perfect agreement with Comphy simulations using consistent defect bands.

NBTI is studied on the same technologies as discussed for PBTI above. The degradation of the plain 5 nm ISSG SiO_2 device can be captured well with similar defect bands as in the previous NBTI studies in Subsections 3.1 and 3.2 as shown in the first part of Fig. 23. The degradation of the device with the additional HfO_2 layer on top is consistent with these defects and increases further due to the deep defect band in the HfO_2 . The shallow defects in the HfO_2 cannot capture electrons at NBTI conditions, hence, are not characterized in this part. While the deep defects in the HfO_2 capture electrons from the gate during recovery after PBTI stress, the same defects can emit electrons during recovery after NBTI stress. This causes the aforementioned anomalous shift of V_{th} towards positive voltages during NBTI stress. While the effect is rather small for the device without the Al_2O_3 layer (second part of Fig. 23), the difference of the alignment in energy due to the Al_2O_3 layer again supports this effect. In fact, in the last recovery phase at low stress voltage a small degradation during recovery (anomalous degradation) can be observed (see last part of Fig. 23).

In another split of this technology the Al_2O_3 layer is selectively removed and a reliability anneal is conducted. Without the Al_2O_3 layer on top, the alignment of the deep defects in the HfO_2 with the Fermi level of the gate becomes again tighter. In perfect agreement with the simulations above, this reduces the anomalous degradation as shown in Fig. 24. Possibly, the diffusion of the aluminum during the anneal affects the defects leading to a slightly different degradation of these devices compared to the one with no Al_2O_3 process step. Accordingly, the life time simulations (see Fig. 25) of the splits without Al_2O_3 and with the removed Al_2O_3 are similar, while the devices with Al_2O_3 in place shows a distinct life time.

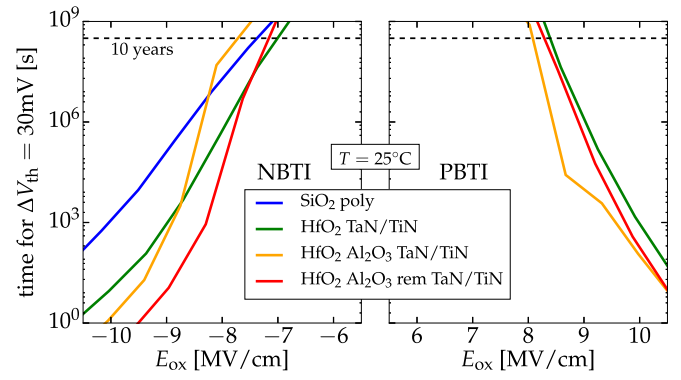


Fig. 25. The simulated life time of the four technologies analyzed in this subsection. Due to the small density of shallow defects in the SiO_2 layer, the PBTI life time of the plain SiO_2 devices is beyond this scale (10^9 s). The technology with the Al_2O_3 layer on top behaves quite differently because of the distortion of the energy alignments, while the small difference of the other two high- κ technologies is due to an anneal and possibly the diffusion of aluminum.

3.4. Extracted defect bands

Four oxide defect bands were extracted in this study as summarized in Fig. 26 and listed in detail in the appendix in Table 7. Since there are stress conditions where not every band contributes to the degradation, the extraction has to be based on carefully designed experiments on both, nMOS and pMOS devices. This yields accurate and consistent defect properties, meaning that a device with these four bands gives consistent results for various PBTI and NBTI conditions.

In SiO_2 we have confirmed the frequently reported deep defects about 1.35 eV below the Si mid gap with a rather high defect density, dominating the recoverable component of NBTI [11, 16]. This defect band appears less pronounced in ISSG SiO_2 , maybe related to the limited thermal budget. Processes with higher thermal budget all show very similar defect properties.

The shallow defects in SiO_2 about 1 eV above Si mid gap have a very low defect density. They are not crucial for usual reliability considerations and rarely studied. Still, there is clear evidence as shown in Subsection 3.3 where they give a PBTI response on a plain SiO_2 oxide. Experimental PBTI data on thin SiON devices stressed at rather high oxide fields is in line with this observation [46].

In HfO_2 a shallow defect band is commonly observed since it severely affects life time at PBTI conditions. In line with our previous study we see a trend of this defect band shifting towards higher energies after anneals [16]. While the mean trap level is around 0.8 eV for technologies without a dedicated reliability anneal, it is close to 1.2 eV above Si mid gap for those with such an anneal.

The deep defects in the HfO_2 have a considerable density, however, in many technologies they are not important due to their deep trap levels. As shown in Subsection 3.3 there are gate stacks where they can have a severe effect and they have to be considered accordingly. The removal of the Al_2O_3 layer does not restore the behavior completely

and we observe slightly lower trap levels and reduced relaxation barriers after processes where Al_2O_3 is involved. A careful study with broader experimental data is necessary to elaborate the effect of annealing and diffusion of aluminum here.

4. Conclusions

Reliability phenomena increasingly dictate advances in the semiconductor industry. This led to intensive research which revealed fundamental oxide degradation mechanisms. Detailed models were proposed which try to capture the common root source of various reliability phenomena, making such universal physical models very attractive. However, adopting these models for standard reliability analyses is difficult because of their inherent complexity. The Comphy framework we have presented here targets the sweet spot between “fundamental physical mechanisms” and “fast, convenient, and scriptable tool”. This framework computes V_{th} of MOS structures with physical channel properties and arbitrary physical gate stacks based on an effective 2-state NMP model for the recoverable component and a simple double-well model for the quasi-permanent part.

We have demonstrated its capabilities to a unified modeling of BTI on three distinct technologies. AC modeling was demonstrated on a commercial 130 nm SiON technology. Long-term BTI and life time

extrapolation was investigated on a commercial 28 nm high- κ technology. Finally, different splits of a technology for DRAM periphery devices were studied and the anomalous degradation due to a thin Al_2O_3 layer on top of a high- κ stack was investigated.

All simulations on both pMOS and nMOS devices use consistent defect bands and all simulations can be fully reproduced with the parameters listed in Tables 6 and 7 using Comphy 1.0 [47]. We confirmed that NBTI is dominated by a deep defect band in the SiO_2 and that PBTI is governed by shallow defects in the HfO_2 . Additionally, we found a shallow defect band in SiO_2 which is responsible for weak PBTI and a deep defect band in HfO_2 which can affect devices with advanced gate stacks.

Acknowledgments

Stimulating discussions with Hans Reisinger, Gunnar Rott, Alexander Grill, Adrian Vaisman Chasin, Al-Moatasem El-Sayed, Lars-Åke Ragnarsson, Hiroaki Arimura, Franz Schanovsky, and Wolfgang Goes are gratefully acknowledged. The research leading to these results has received funding from the FFG project no 861022 and the Austrian Science Fund (FWF) project no i2606-N30. GTS (Global TCAD Solutions) is acknowledged for support.

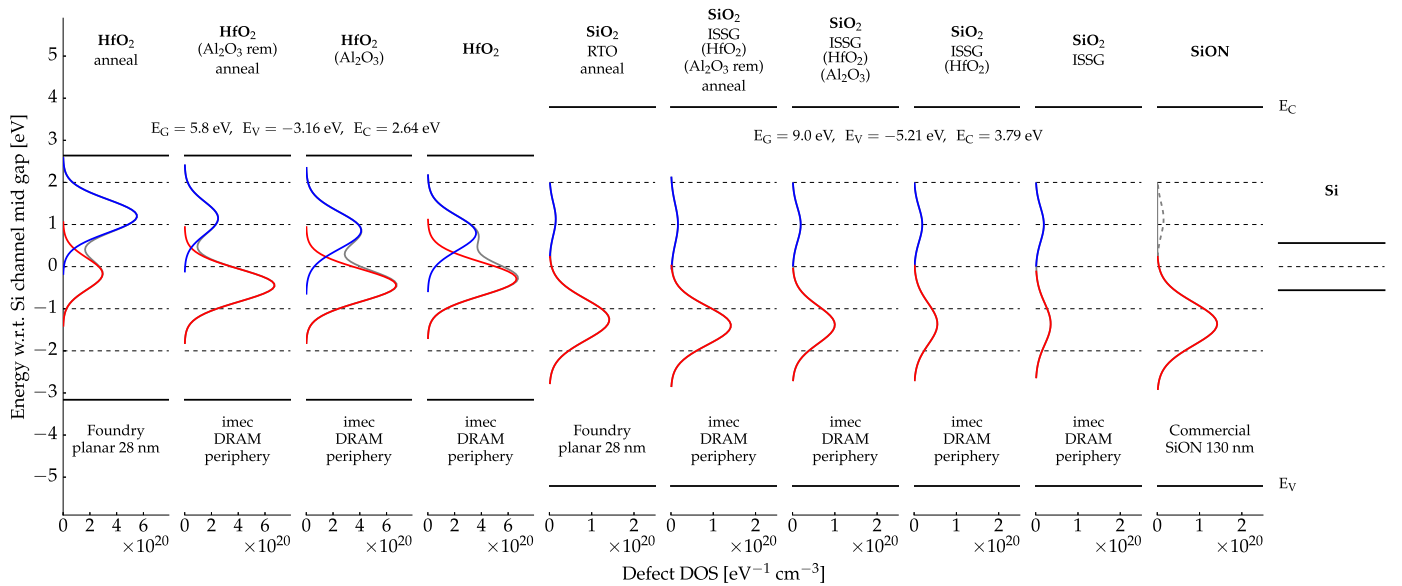


Fig. 26. The defect bands extracted in HfO_2 and SiO_2 are similar across all technologies studied in this work and enable unified modeling of BTI on pMOS and nMOS devices. Most prominent is the shallow band in the HfO_2 which is largely responsible for PBTI and the deep band in SiO_2 which governs NBTI degradation. Still, there is clear evidence for a deep band in HfO_2 and a shallow band in SiO_2 . Regarding the impact of processes on the defect properties, a clear shift of the shallow defects in HfO_2 towards higher defect levels can be observed after a reliability anneal. Furthermore, there seems to be a correlation of the thermal budget with the density of the deep defects in SiO_2 and processes involving Al_2O_3 seem to affect the deep band in HfO_2 . Dedicated studies are required to elaborate these observations.

Appendix A

Table 7

Details of the technologies presented in this study together with all technology dependent Comphy parameters. The same defect parameters were used for pMOS and nMOS transistors of the same technology. Material default parameters which are the same for all technologies are listed in [Tables 1](#) and [6](#). The capture cross sections are $\sigma_{0,n} = \sigma_{0,p} = 2 \times 10^{-19} \text{ cm}^{-2}$.

			Commercial SiON 130 nm	imec DRAM periphery	imec DRAM periphery	imec DRAM periphery	imec DRAM periphery	Foundry planar 28 nm
Technology details	SiO ₂		SiON	ISSG	ISSG	ISSG	ISSG	RTO
	HfO ₂		-	-	✓	✓	✓	✓
	Al ₂ O ₃		-	-	-	✓	removed	-
	PDA		-	-	-	-	✓	✓
	gate		poly	poly	TaN/TiN	TaN/TiN	TaN/TiN	TiN
	EOT	nm	1.43	5	4.94	5.07	4.9	1.41
	V _{th,0}	V	-	0.375	0.952	1.25	1.11	0.438
	nMOS							
	V _{th,0}	V	-0.431	-0.469	-0.929	-0.759	-0.755	-0.404
	pMOS							
	V _{G,fb}	V	-	-0.921	-0.516	-0.35	-0.464	-0.826
	nMOS							
	V _{G,fb}	V	0.532	1.04	0.579	0.716	0.705	0.523
	pMOS							
Input parameters	N _A nMOS	cm ⁻³	-	2.8 × 10 ¹⁷	5 × 10 ¹⁷	6.77 × 10 ¹⁷	6.77 × 10 ¹⁷	1.59 × 10 ¹⁸
	N _D pMOS	cm ⁻³	2 × 10 ¹⁷	5.5 × 10 ¹⁷	5.6 × 10 ¹⁷	4.9 × 10 ¹⁷	4.9 × 10 ¹⁷	1.4 × 10 ¹⁷
	ΔE _w	eV	-	-0.48	-0.06	0.114	0	-0.34
	nMOS							
	ΔE _w	eV	0.1	0.581	0.12	0.261	0.25	0.1
	pMOS							
	x _{SiO₂}	nm	2.2	5	4.55	4.55	4.55	1
	x _{HfO₂}	nm	-	-	2	1.8	1.8	2.1
	x _{Al₂O₃}	nm	-	-	-	0.4	-	-
Shallow SiO ₂	N _T	cm ⁻³	-	1.93 × 10 ¹⁹	1.93 × 10 ¹⁹	1.93 × 10 ¹⁹	1.65 × 10 ¹⁹	1.5 × 10 ¹⁹
	⟨E _T ⟩ ± σ _{ET}	eV	-	0.998 ± 0.162	0.998 ± 0.162	0.998 ± 0.162	1.01 ± 0.218	1.13 ± 0.15
	⟨S⟩ ± σ _S	eV	-	4.93 ± 1.99	4.93 ± 1.99	4.93 ± 1.99	3.82 ± 1.36	3.82 ± 1.36
	R	1	-	0.437	0.437	0.437	0.407	0.407
Deep SiO ₂	N _T	cm ⁻³	1.42 × 10 ²⁰	3.54 × 10 ¹⁹	5.5 × 10 ¹⁹	1 × 10 ²⁰	1.42 × 10 ²⁰	1.42 × 10 ²⁰
	⟨E _T ⟩ ± σ _{ET}	eV	-1.36 ± 0.26	-1.36 ± 0.24	-1.36 ± 0.24	-1.38 ± 0.2	-1.4 ± 0.21	-1.26 ± 0.24
	⟨S⟩ ± σ _S	eV	7.95 ± 3.5	5.63 ± 2.67	5.63 ± 2.67	5.63 ± 2.67	5.63 ± 2.67	5.63 ± 2.67
	R	1	2.59	2.25	2.25	2.25	2.25	1.8
Shallow HfO ₂	N _T	cm ⁻³	-	-	3.61 × 10 ²⁰	4.11 × 10 ²⁰	2.5 × 10 ²⁰	5.52 × 10 ²⁰
	⟨E _T ⟩ ± σ _{ET}	eV	-	-	0.794 ± 0.169	0.857 ± 0.189	1.15 ± 0.15	1.2 ± 0.156
	⟨S⟩ ± σ _S	eV	-	-	6.98 ± 0.511	6.45 ± 0.34	6 ± 0.6	3.19 ± 0.77
	R	1	-	-	0.692	0.659	0.61	0.587
Deep HfO ₂	N _T	cm ⁻³	-	-	6.63 × 10 ²⁰	6.72 × 10 ²⁰	6.72 × 10 ²⁰	2.95 × 10 ²⁰
	⟨E _T ⟩ ± σ _{ET}	eV	-	-	-0.292 ± 0.158	-0.444 ± 0.15	-0.444 ± 0.15	-0.17 ± 0.14
	⟨S⟩ ± σ _S	eV	-	-	5.81 ± 1.74	3.55 ± 0.741	3.55 ± 0.741	6.5 ± 1.99
	R	1	-	-	1	1	1	0.514
Double well	N _T	cm ⁻²	6.5 × 10 ¹³	4.5 × 10 ¹³	4.5 × 10 ¹³	4.5 × 10 ¹³	4.5 × 10 ¹³	4.5 × 10 ¹³
	⟨ε ₁ ⟩ ± σ _{ε1}	eV	2.73 ± 0.43	2.51 ± 0.376	2.46 ± 0.376	2.34 ± 0.395	2.33 ± 0.376	2.32 ± 0.376
	⟨ε ₂ ⟩ ± σ _{ε2}	eV	2.75 ± 0.7	1.9 ± 0.5	1.9 ± 0.5	1.9 ± 0.5	1.9 ± 0.5	1.77 ± 0.5
	k ₀	s ⁻¹	1 × 10 ¹³	1 × 10 ¹³	1 × 10 ¹³	1 × 10 ¹³	1 × 10 ¹³	1 × 10 ¹³
	γ	eV	7 × 10 ⁻¹⁰	4.8 × 10 ⁻¹⁰	4.8 × 10 ⁻¹⁰	4.5 × 10 ⁻¹⁰	4.5 × 10 ⁻¹⁰	6.8 × 10 ⁻¹⁰
		m/V						

References

- [1] B. Deal, M. Sklar, A.S. Grove, E.H. Snow, Characteristics of the surface-state charge (Q_{ss}) of thermally oxidized silicon, *J. Electrochem. Soc.* 114 (3) (1967) 266.
- [2] J.H. Stathis, S. Mahapatra, T. Grasser, Controversial issues in negative bias temperature instability, *Microelectron. Reliab.* 81 (2018) 244–251.
- [3] J. Stathis, Dissociation kinetics of hydrogen-passivated (100) Si/SiO₂ interface defects, *J. Appl. Phys.* 77 (12) (1995) 6205–6207.
- [4] J. Conley Jr., P. Lenahan, A. Lelis, T. Oldham, Electron spin resonance evidence that E_v' centers can behave as switching oxide traps, *IEEE Trans. Nucl. Sci.* 42 (6) (1995) 1744–1749.
- [5] S. Mahapatra, M. Alam, A predictive reliability model for PMOS bias temperature degradation, *Proc. Intl. Electron Devices Meeting (IEDM)* (2002) 505–508.
- [6] K. Huang, A. Rhys, Theory of light absorption and non-radiative transitions in F-centers, *Proc. R. Soc. A* 204 (1950) 406–423.
- [7] D. Lang, C. Henry, Nonradiative recombination at deep levels in GaAs and GaP by lattice-relaxation multiphonon emission, *Phys. Rev. Lett.* 35 (22) (1975) 1525–1528.
- [8] M. Kirton, M. Uren, Noise in solid-state microstructures: a new perspective on individual defects, interface states and low-frequency (1/f) noise, *Adv. Phys.* 38 (4) (1989) 367–486.
- [9] T. Grasser, Stochastic charge trapping in oxides: from random telegraph noise to bias temperature instabilities, *Microelectron. Reliab.* 52 (2012) 39–70.
- [10] T. Grasser, K. Rott, H. Reisinger, M. Waltl, J. Franco, B. Kaczer, A unified perspective of RTN and BTI, *Proc. Intl. Rel. Phys. Symp. (IRPS)*, 2014 4A.5.1–4A.5.7.
- [11] G. Rzepa, M. Waltl, W. Goes, B. Kaczer, J. Franco, T. Chiarella, N. Horiguchi, T. Grasser, Complete extraction of defect bands responsible for instabilities in n and pFinFETs, *IEEE Symposium on VLSI Technology Digest of Technical Papers*, 2016, pp. 208–209.
- [12] T. Grasser, M. Waltl, G. Rzepa, W. Goes, Y. Wimmer, A. El-Sayed, A. Shluger, H. Reisinger, B. Kaczer, The “permanent” component of NBTI revisited: saturation, degradation-reversal, and annealing, *Proc. Intl. Rel. Phys. Symp. (IRPS)*, June 2016.
- [13] L. Vandelli, L. Larcher, D. Veksler, A. Padovani, G. Bersuker, K. Matthews, A charge-trapping model for the Fast Component of Positive Bias Temperature Instability (PBTI) in High-κ Gate-Stacks, *IEEE Trans. Electron Devices* 61 (7) (2014) 2287–2293.
- [14] T. Grasser, M. Waltl, Y. Wimmer, W. Goes, R. Kosik, G. Rzepa, H. Reisinger, G. Pobegen, A. El-Sayed, A. Shluger, B. Kaczer, Gate-sided hydrogen release as the origin of permanent NBTI degradation: from single defects to lifetimes, *Proc. Intl. Electron Devices Meeting (IEDM)*, Dec. 2015, pp. 401–404.
- [15] M. Duan, J.F. Zhang, Z. Ji, W.D. Zhang, D. Vigar, A. Asenov, L. Gerrer, V. Chandra, R. Aitken, B. Kaczer, Insight into electron traps and their energy distribution under positive bias temperature stress and hot carrier aging, *IEEE Trans. Electron Devices* 63 (9) (2016).
- [16] G. Rzepa, J. Franco, A. Subirats, M. Jech, A. Chasin, A. Grill, M. Waltl, T. Knobloch, D. Linten, B. Kaczer, T. Grasser, Efficient physical defect model applied to PBTI in high-κ stacks, *IEEE International Reliability Physics Symposium Proceedings*, 2017, pp. 1–6.
- [17] L. Gerrer, S. Ling, S.M. Amoroso, P. Asenov, A.L. Shluger, A. Asenov, From atoms to product reliability: toward a generalized multiscale simulation approach, *J. Comput. Electron.* 12 (4) (2013) 638–650.
- [18] C. Kaneta, T. Yamasaki, T. Uchiyama, T. Uda, K. Terakura, Structure and electronic property of Si(100)/SiO₂ interface, *Microelectron. Eng.* 48 (1999) 117–120.
- [19] Y. Yamashita, S. Yamamoto, K. Mukai, J. Yoshinobu, Y. Harada, T. Tokushima, T. Takeuchi, Y. Takata, S. Shin, K. Akagi, S. Tsuneyuki, Direct observation of site-specific valence electronic structure at the SiO₂/Si interface, *Phys. Rev. B* 73 (4) (2006) 045336.
- [20] Z. Huiwen, L. Yongsong, M. Lingfeng, S. Jingqin, Z. Zhiyan, T. Weihua, Theoretical study of the SiO₂/Si interface and its effect on energy band profile and MOSFET gate tunneling current, *J. Semicond.* 31 (8) (2010) 082003.
- [21] O. Sharia, A.A. Demkov, G. Bersuker, B.H. Lee, Theoretical study of the insulator/insulator interface: band SiO₂/HfO₂ junction, *Phys. Rev. B* 75 (3) (2007) 035306.
- [22] J.E. Lang, F.L. Madarasz, P.M. Hemenger, Temperature dependent density of states effective mass in nonparabolic p-type silicon, *J. Appl. Phys.* 54 (6) (1983) 3612.
- [23] W.B. Joyce, R.W. Dixon, Analytic approximations for the Fermi energy of an ideal Fermi gas, *Appl. Phys. Lett.* 31 (5) (1977) 354–356.
- [24] M.A. Green, Intrinsic concentration, effective densities of states, and effective mass in silicon, *J. Appl. Phys.* 67 (6) (1990) 2944–2954.
- [25] S. Sze, *Physics of Semiconductor Devices*, Third, Wiley, New York, 1981.
- [26] K.-U. Giering, C. Sohrmann, G. Rzepa, L. Heis, T. Grasser, R. Jancke, NBTI Modeling in analog circuits and its application to long-term aging simulations, *Proc. Intl. Integrated Reliability Workshop*, 2014, pp. 29–34.
- [27] J.R. Hauser, CVC version 5.0, www.ece.ncsu.edu/research/tools/.
- [28] H. Miki, N. Tega, M. Yamaoka, D.J. Frank, A. Bansal, M. Kobayashi, K. Cheng, C. D'Emic, Z. Ren, S. Wu, J.-B. Yau, Y. Zhu, M.A. Guillorn, D.-G. Park, W. Haensch, E. Leobandung, K. Torii, Statistical measurement of random telegraph noise and its impact in scaled-down high-κ/metal-gate MOSFETs, *Proc. Intl. Electron Devices Meeting (IEDM)*, 2012, pp. 450–453.
- [29] W. Goes, Y. Wimmer, A. El-Sayed, G. Rzepa, M. Jech, A. Shluger, T. Grasser, Modeling of oxide defects in semiconductor devices: connecting first-principles with rate equations, *Microelectron. Reliab.* (2018) (to appear).
- [30] *Bias Temperature Instability for Devices and Circuits*, in: T. Grasser (Ed.), Springer, New York, 2014.
- [31] T. Tewksbury, Relaxation Effects in MOS Devices due to Tunnel Exchange with Near-Interface Oxide Traps, (1992) Ph.D. Thesis, MIT.
- [32] F. Schanovsky, W. Goes, T. Grasser, An advanced description of oxide traps in MOS transistors and its relation to DFT, *J. Comp. Elec.* 9 (3–4) (2010) 135–140.
- [33] E. Bersch, S. Rangan, R.A. Bartynski, E. Garfunkel, E. Vescovo, Band offsets of ultrathin high-κ oxide films with Si, *Phys. Rev. B* 78 (8) (2008) 1–10.
- [34] G. Rzepa, W. Goes, G. Rott, et al., Physical modeling of NBTI: from individual defects to devices, *Proc. Simulation of Semiconductor Processes and Devices*, 2014, pp. 81–84.
- [35] K.-U. Giering, G. Rott, G. Rzepa, H. Reisinger, A. Puppala, T. Reich, W. Gustin, T. Grasser, R. Jancke, Analog-circuit NBTI degradation and time-dependent NBTI variability: an efficient physics-based compact model, *Proc. Intl. Rel. Phys. Symp. (IRPS)*, 2016.
- [36] H. Reisinger, T. Grasser, K. Ermisch, et al., Understanding and modeling AC BTI, *Proc. Intl. Rel. Phys. Symp. (IRPS)*, 2011, pp. 597–604.
- [37] T. Grasser, B. Kaczer, H. Reisinger, P.-J. Wagner, M. Toledano-Luque, On the frequency dependence of the bias temperature instability, *Proc. Intl. Rel. Phys. Symp. (IRPS)*, 2012 XT.8.1–XT.8.7.
- [38] T. Grasser, P.-J. Wagner, H. Reisinger, T. Aichinger, G. Pobegen, M. Nelhiebel, B. Kaczer, Analytic modeling of the bias temperature instability using capture/emission time maps, *Proc. Intl. Electron Devices Meeting (IEDM)*, Dec. 2011 27.4.1–27.4.4.
- [39] H. Reisinger, T. Grasser, W. Gustin, C. Schlünder, The statistical analysis of individual defects constituting NBTI and its implications for modeling DC- and AC-stress, *Proc. Intl. Rel. Phys. Symp. (IRPS)*, May 2010, pp. 7–15.
- [40] B. Kaczer, T. Grasser, P. Roussel, J. Martin-Martinez, R. O'Connor, B. O'Sullivan, G. Groeseneken, Ubiquitous relaxation in BTI stressing - new evaluation and insights, *Proc. Intl. Rel. Phys. Symp. (IRPS)*, 2008, pp. 20–27.
- [41] S. Mukhopadhyay, S. Mahapatra, An experimental perspective of trap generation under BTI stress, *IEEE Trans. Electron Devices* 62 (7) (2015) 2092–2097.
- [42] S. Mukhopadhyay, K. Joshi, V. Chaudhary, N. Goel, S. De, R.K. Pandey, K.V.R.M. Murali, S. Mahapatra, Trap generation in IL and HK layers during BTI/TDD stress in scaled HKMG N and P MOSFETs, *Proc. Intl. Rel. Phys. Symp. (IRPS)*, 2014, pp. 1–11.
- [43] R. O'Connor, V.S. Chang, L. Pantisano, L.-Å. Ragnarsson, M. Aoulaiche, B. O'Sullivan, G. Groeseneken, Anomalous positive-bias temperature instability of high-κ/metal gate devices with Dy₂O₃ capping, *Appl. Phys. Lett.* 93 (5) (2008) 053506.
- [44] M. Toledano-Luque, B. Kaczer, M. Aoulaiche, A. Spessot, P.J. Roussel, R. Ritzenthaler, T. Schram, A. Thean, G. Groeseneken, Analytical model for anomalous positive bias temperature instability in La-based HfO₂ nFETs based on independent characterization of charging components, *Microelectron. Eng.* 109 (2013) 314–317.
- [45] M. Si, H. Wu, S. Shin, W. Luo, N.J. Conrad, W. Wu, J. Zhang, M.A. Alam, P.D. Ye, Anomalous bias temperature instability on accumulation-mode Ge and III-V MOSFETs, *Proc. Intl. Rel. Phys. Symp. (IRPS)* (2017) 1–6.
- [46] E. Cartier, A. Kerber, T. Ando, M.M. Frank, K. Choi, S. Krishnan, B. Linder, K. Zhao, F. Monsieur, J. Stathis, V. Narayanan, Fundamental aspects of HfO₂-based high-κ metal gate stack reliability and implications on t_{inv}-scaling, *Proc. Intl. Electron Devices Meeting (IEDM)* (2011) 18.4.1–18.4.4.
- [47] Comphy version 1.0 (www.comphy.eu), Institute for Microelectronics/TU Wien and imec, 2018, www.comphy.eu.